



THE UNIVERSITY *of* EDINBURGH

Edinburgh Research Explorer

Directional sources in wave-based acoustic simulation

Citation for published version:

Bilbao, S & Hamilton, B 2019, 'Directional sources in wave-based acoustic simulation', *IEEE/ACM Transactions on Audio, Speech and Language Processing*, vol. 27, no. 2, pp. 415-428.
<https://doi.org/10.1109/TASLP.2018.2881336>

Digital Object Identifier (DOI):

[10.1109/TASLP.2018.2881336](https://doi.org/10.1109/TASLP.2018.2881336)

Link:

[Link to publication record in Edinburgh Research Explorer](#)

Document Version:

Peer reviewed version

Published In:

IEEE/ACM Transactions on Audio, Speech and Language Processing

Publisher Rights Statement:

© 2018 IEEE

General rights

Copyright for the publications made accessible via the Edinburgh Research Explorer is retained by the author(s) and / or other copyright owners and it is a condition of accessing these publications that users recognise and abide by the legal requirements associated with these rights.

Take down policy

The University of Edinburgh has made every reasonable effort to ensure that Edinburgh Research Explorer content complies with UK legislation. If you believe that the public display of this file breaches copyright please contact openaccess@ed.ac.uk providing details, and we will remove access to the work immediately and investigate your claim.



Directional Sources in Wave-based Acoustic Simulation

*Stefan Bilbao, *Senior Member, IEEE* and Brian Hamilton, *Member, IEEE*

Abstract—Volumetric wave-based acoustic simulation relies on the complete solution to the 3D wave equation over a spatial grid. Detailed modeling of sources, however, requires interpolation over the grid, which is complicated by the directional character of the source itself. In this article, a new model of point sources of arbitrary directivity and location with respect to an underlying grid is presented. The model is framed in the spatio-temporal domain directly through the differentiation of Dirac distributions, leading to a spatial Fourier-based approximation strategy. Various approximants are presented, of both separable and non-separable type, and allowing for optimisation over a specified wavenumber range. Such approximants are then employed in a finite difference time domain setting, yielding numerical results for sources of various types, which are then compared against exact solutions.

Index Terms—room acoustics, finite difference time domain method, multipole modeling, source modeling.

I. INTRODUCTION

Volumetric time domain modeling of acoustic spaces, for applications in architectural acoustics and virtualisation, was first proposed in the early 1990s [1]–[3]. Such methods are based on full wave-based modeling of the acoustic field, in contrast with geometric methods such as ray tracing [4] or the image source method [5], which are valid in the limit of high frequencies. At first confined to deal with problems defined over small geometries, and for low frequencies, computational power has increased to the extent that wave-based methods may now be used to simulate large acoustic spaces, typically on GPUs [6], [7] and at typical audio sampling frequencies [8], [9]. Parallelisability of such algorithms is a major concern, and thus methods defined over regular grids, such as the finite difference time domain (FDTD) method [10], [11] are a natural choice, with generalisations such as the finite volume time domain method [12], [13] useful in order to handle irregular geometries and realistic wall impedances in a provably stable manner [14], [15]. Such methods have the property of a local update at a given grid point, based on values over a set of nearby locations, or stencil; other non-local methods, such as pseudo-spectral methods have also seen some interest [16], [17].

The modeling of acoustic sources in FDTD has been approached by various authors, and interest has been mainly in the modeling of point-like monopoles, activating a single node in a grid. The emphasis has been on distinct models (soft-source, hard-source and transparent-source [18]–[20]), and, in

particular, filtering strategies applied in order to obtain reasonable impulse responses [21]. Directional sources have also been described, sometimes employing differences between neighbouring values on the grid [22], [23], and through direct comparison against specified directivity patterns [24]. The dual problem of receiver directivity in waveguide meshes (which are equivalent to FDTD) has been described in [25], [26]. Sources within spectral approximations have been discussed in [27].

In most cases above, which deal with discretisation directly, there is an absence of an underlying model of the source itself for the continuous problem (with some exceptions [7]). Such models do appear in the acoustics literature, often framed in terms of the free-space solution to the wave equation (and its derivatives) under steady sinusoidal excitation conditions [28]. Considering the simulation of realistic spaces and sources, where (a) free-space solutions do not hold due to the finite extent of the problem domain, (b) sources may have a complex directional character and be mobile or dynamic, and furthermore (c) may not be aligned with grid points or axes in an FDTD setting, a more general model is desirable. Such generality follows from a model framed as an inhomogeneous wave equation with a source term depending on a localised distribution (such as a Dirac delta function or its derivatives), and thus suitable for direct spatio-temporal simulation. The problem, then, becomes one of the representation of such localised distributions over a grid [29], [30], which requires some care when audio considerations come into play.

In this article, a new localised source model is presented, allowing for arbitrary source placement and directivity, as well as various approaches to discretisation. The 3D wave equation is presented in Section II, followed by a model of pointwise multipole sources of arbitrary order in Section III. Different families of approximations to the 3D Dirac delta function and its derivatives are presented in Section IV, and basic finite difference schemes for the 3D wave equation in Section V. Numerical results appear in Section VI, and some concluding remarks and perspectives follow in Section VII. Some relevant tensor definitions and identities appear in the Appendix. Preliminary results have appeared in [31].

II. THE 3D WAVE EQUATION

The usual starting point for models of wave propagation in room acoustics applications is the linearised system

$$\rho \partial_t \mathbf{v} + \nabla p = \mathbf{0} \quad (1a)$$

$$\frac{1}{\rho c^2} \partial_t p + \nabla \cdot \mathbf{v} = 0. \quad (1b)$$

S. Bilbao and B. Hamilton are with the Acoustics and Audio Group, University of Edinburgh, Room 1602, JCMB, King's Buildings, Edinburgh, UK, EH9 3JZ. Tel: +44 131 651 7043, email: sbilbao@staffmail.ed.ac.uk. Both are supported by the European Research Council, under grant number ERC-2016-PoC-737574-WRAM.

Here, the scalar quantity $p(\mathbf{x}, t)$ and the three-vector $\mathbf{v}(\mathbf{x}, t)$ are the acoustic pressure and vector particle velocity, respectively. Both are defined for time $t \geq 0$, and in terms of coordinates $\mathbf{x} = [x_1, x_2, x_3] \in \mathcal{D} \subset \mathbb{R}^3$. ∂_t represents partial differentiation with respect to time t , and ∇ and $\nabla \cdot$ are the three-dimensional (3D) gradient and divergence operations, respectively. ρ and c are the density of air and wave speed respectively at a given temperature, and assumed constant here. $\mathbf{0}$ is the null three vector. Equations (1a) and (1b) correspond, respectively, to pointwise conservation of momentum and mass in the acoustic field. In this article, which is concerned with source modeling, the domain will be assumed to be infinite, so that $\mathcal{D} = \mathbb{R}^3$, and thus wall conditions need not be taken into consideration.

The 3D wave equation may be deduced from (1) through the elimination of the velocity variable \mathbf{v} :

$$\frac{1}{c^2} \partial_t^2 p - \Delta p = 0. \quad (2)$$

Here $\Delta = \nabla \cdot \nabla$ is the 3D Laplacian operator. (2) above is written in terms of the acoustic pressure p alone, although it is possible to arrive at a similar form written in terms of the velocity potential—see, e.g., [32]. Both the first order system (1) and the 3D wave equation can be used as starting points for volumetric time-stepping methods such as FDTD. Here, the second order form will be employed.

III. DIRECTIONAL POINT SOURCE MODELING

Suppose a source is located at coordinates $\mathbf{x}_S = [x_{S,1}, x_{S,2}, x_{S,3}]$. It is useful, before presenting a model of the source itself, to introduce source-centred coordinates \mathbf{r} as

$$\mathbf{r} = \mathbf{x} - \mathbf{x}_S, \quad (3)$$

or, in terms of distance r and azimuth and inclination angles θ and ϕ between the source and field point as $\mathbf{r} = r\mathbf{d}$, where

$$r = |\mathbf{r}| \quad \mathbf{d} = [\sin(\phi) \cos(\theta) \quad \sin(\phi) \sin(\theta) \quad \cos(\phi)]. \quad (4)$$

In the setting of numerical simulation, the underlying absolute coordinates \mathbf{x} will be retained for the definition of a spatial grid, and relative coordinates \mathbf{r} for approximations to the source. The definitions of the spatial differential operators ∇ , $\nabla \cdot$ and Δ may be interpreted in terms of either set of coordinates, and thus will be left unlabelled here.

A. Monopole Sources

Source terms are not included in (1) above. A standard model of a pointwise monopole source [28], located at absolute coordinates \mathbf{x}_S may be written through a modification of (1b), and in source-centred coordinates \mathbf{r} , as

$$\frac{1}{\rho c^2} \partial_t p + \nabla \cdot \mathbf{v} = Q \delta^{(3)}(\mathbf{r}). \quad (5)$$

Here, $Q = Q(t)$ is the so-called source strength, with dimensions of volume velocity. $\delta^{(3)}(\mathbf{r})$ is a 3D Dirac delta function centered at the absolute coordinates \mathbf{x}_S ; formally, it may be separated as

$$\delta^{(3)}(\mathbf{r}) = \delta^{(1)}(x_1 - x_{S,1}) \delta^{(1)}(x_2 - x_{S,2}) \delta^{(1)}(x_3 - x_{S,3}), \quad (6)$$

where $\delta^{(1)}$ represents the one-dimensional (1D) Dirac distribution. When combined with (1a), the following inhomogeneous wave equation results [28]:

$$\frac{1}{c^2} \partial_t^2 p - \Delta p = \rho \dot{Q} \delta^{(3)}(\mathbf{r}), \quad (7)$$

where here, \dot{Q} represents the ordinary time derivative of Q . Under quiescent initial conditions, the inhomogeneous equation (7) has the well-known solution

$$p(\mathbf{r}, t) = \frac{\rho \dot{Q}(t - r/c)}{4\pi r}. \quad (8)$$

Such a model can be viewed as resulting from a uniformly vibrating sphere, in the limit of vanishing source radius. It is not to be viewed as a boundary—that is, it is capable of producing acoustic energy, but not scattering it.

B. Dipole Sources

Basic models of dipole sources are often written in terms of closely-spaced pairs of monopole sources of opposite strength [32]. It is also possible to begin from the addition of a pointwise directional source term in (1a), as

$$\rho \partial_t \mathbf{v} + \nabla p = \mathbf{n}_D F \delta^{(3)}(\mathbf{r}). \quad (9)$$

Here, $F = F(t)$ is a scalar signal with dimensions of Newtons, again acting at absolute source coordinates \mathbf{x}_S , and with direction \mathbf{n}_D , where \mathbf{n}_D is a unit amplitude 3-vector, defined in terms of azimuth and inclination angles θ_D and ϕ_D as

$$\mathbf{n}_D = [\sin(\phi_D) \cos(\theta_D) \quad \sin(\phi_D) \sin(\theta_D) \quad \cos(\phi_D)]. \quad (10)$$

Again, through recombination with (1b), an inhomogeneous wave equation results [28]:

$$\frac{1}{c^2} \partial_t^2 p - \Delta p = -F \mathbf{n}_D \cdot \nabla \delta^{(3)}(\mathbf{r}), \quad (11)$$

where $\nabla \delta^{(3)}$ is the gradient of $\delta^{(3)}$ in the distributional sense.

The solution to (11), again under zero initial conditions, is

$$p(\mathbf{r}, t) = \frac{\mathbf{d} \cdot \mathbf{n}_D}{4\pi r^2} \left(\frac{r}{c} \partial_t + 1 \right) F(t - r/c). \quad (12)$$

C. General Multipole Sources

The introduction of higher-order multipole sources is often approached through the combination of simpler combinations of monopoles and dipoles [28]. A more general approach is to make use of source terms which result from multiple differentiation of the Dirac delta function:

$$\frac{1}{c^2} \partial_t^2 p - \Delta p - f = 0 \quad f(\mathbf{r}, t) = \sum_{q=0}^{\infty} f^{(q)}, \quad (13)$$

where

$$f^{(q)} = \Psi^{(q)} \cdot \underbrace{\left(\nabla^q \delta^{(3)}(\mathbf{r}) \right)}_{\mathbf{r}^{(q)}}. \quad (14)$$

Here, $\Psi^{(q)} = \Psi_{\gamma}^{(q)}(t)$ is a q th-order tensor indexed by the q -vector $\gamma = [\gamma_1, \dots, \gamma_q]$, where $\gamma_l, l = 1, \dots, q$ takes on the value 1, 2 or 3. See the Appendix. ∇^q , the q th power of the gradient operation, as defined in (69) is also a q th-order

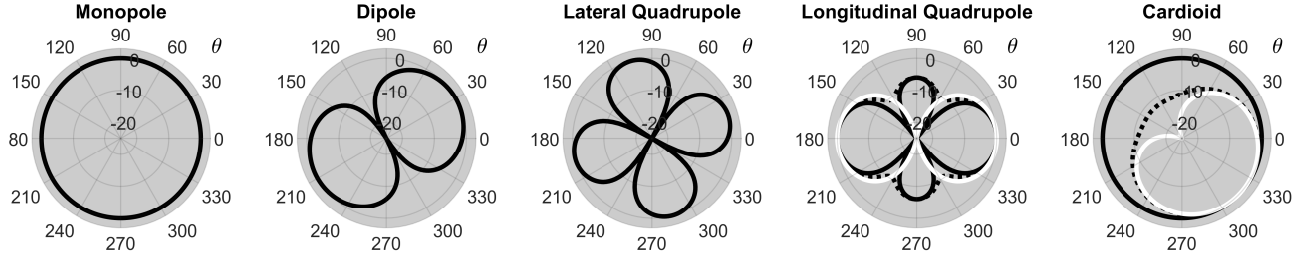


Fig. 1: Directivity for various sources in dB, as a function of θ , for $\phi = \pi/2$: the monopole, the dipole, with $[\phi_D, \theta_D] = [\pi/2, \pi/6]$, a lateral quadrupole, with $[\phi_Q, \theta_Q] = [\pi/2, \pi/3]$ and $[\hat{\phi}_Q, \hat{\theta}_Q] = [\pi/2, -\pi/6]$, a longitudinal quadrupole with $\phi_Q = \hat{\phi}_Q = \pi/2$ and $\theta_Q = \hat{\theta}_Q = 0$, and an asymmetric source as described in Section III-E with $[\phi_D, \theta_D] = [\pi/2, -\pi/4]$. In the last two cases, directivity is dependent on the parameter $\eta = r\omega/c$, shown in the near field for $\eta = 0.01$ (black), $\eta = 1$ (dotted) and in the far field for $\eta = 100$ (white).

tensor, indexed similarly. The operation $\cdot^{(q)}$ represents a q -fold contracted inner product, as defined in (68). For a given q , the term in the series appearing in (13) represents a general combination of q th-order spatial derivatives of the Dirac delta function, represented here as the q th-order tensor $\Upsilon^{(q)}$.

The general solution to (13) may be derived as

$$p(\mathbf{r}, t) = \frac{1}{4\pi} \sum_{q=0}^{\infty} \nabla^q \cdot^{(q)} \left(\frac{\Psi^{(q)}(t - r/c)}{r} \right). \quad (15)$$

If the forcing functions $\Psi^{(q)}$ are proportional to Dirac delta functions (in time), the Fourier transform of the solution above may be viewed as the free-space Green's function for the Helmholtz equation, under the forcing term as given in (13).

The inhomogeneous equations (7) and (11) corresponding to the point monopole and dipole may be recovered from (13) above by using, in isolation, $\Psi^{(0)} = \rho\dot{Q}$ and $\Psi^{(1)} = -\mathbf{n}_D F$. The general solutions (8) and (12) for the monopole and dipole also follow from the general form from (15) above, under the choices given above, again employed in isolation.

D. Quadrupole Sources

A useful special case, beyond that of the monopole or dipole, is that of the general quadrupole, characterised by the source 2-tensor $\Psi^{(2)}$. Well-known examples of the longitudinal and lateral quadrupole follow from the representation

$$\Psi^{(2)} = \frac{\psi^{(2)}}{2} (\mathbf{n}_Q \otimes \hat{\mathbf{n}}_Q + \hat{\mathbf{n}}_Q \otimes \mathbf{n}_Q), \quad (16)$$

which is written in terms of a scalar quadrupole amplitude $\psi^{(2)}(t)$, and the outer product (indicated by \otimes) of two unit-length column 3-vectors \mathbf{n}_Q and $\hat{\mathbf{n}}_Q$. These may be written in terms of the azimuth/inclination angle pairs $[\theta_Q, \phi_Q]$ and $[\hat{\theta}_Q, \hat{\phi}_Q]$ as in the case of the dipole in (10). If $\mathbf{n}_Q = \hat{\mathbf{n}}_Q$, then a longitudinal quadrupole results, oriented in direction \mathbf{n}_Q . If $\mathbf{n}_Q \perp \hat{\mathbf{n}}_Q$, then a lateral quadrupole results, oriented in direction $\mathbf{n}_Q \times \hat{\mathbf{n}}_Q$. Though these are generally the only cases that appear in the acoustics literature, the representation in (16) does not span the range of possible quadrupoles, for a general 2-tensor $\Psi^{(2)}$.

For the special case of a quadrupole which may be written in the form (16) above, the general solution is

$$p(\mathbf{r}, t) = -\frac{(\mathbf{n}_Q \cdot \hat{\mathbf{n}}_Q) \left(\frac{r}{c} \dot{\psi}^{(2)} + \psi^{(2)} \right)}{4\pi r^3} + \frac{(\mathbf{n}_Q \cdot \mathbf{d})(\hat{\mathbf{n}}_Q \cdot \mathbf{d}) \left(\frac{r^2}{c^2} \ddot{\psi}^{(2)} + 3\frac{r}{c} \dot{\psi}^{(2)} + 3\psi^{(2)} \right)}{4\pi r^3}, \quad (17)$$

where $\psi^{(2)}$ and its temporal derivatives are evaluated at time $t - r/c$.

E. Asymmetric Sources

For the model given in (13), if only one term, of order q is included, then the solution exhibits symmetry (or antisymmetry) about $\mathbf{r} = \mathbf{0}$, as

$$p(\mathbf{r}, t) = (-1)^q p(-\mathbf{r}, t). \quad (18)$$

Sources with an asymmetric character require multiple terms in (13). As a simple example, consider (13) with terms in $q = 0$ and $q = 1$, and where $\psi^{(0)}$ and $\Psi^{(1)} = \psi^{(1)} \mathbf{n}_D$, for some unit 3-vector \mathbf{n}_D , are related by

$$\psi^{(0)}(t) = \frac{1}{c} \dot{\psi}^{(1)}(t). \quad (19)$$

As in the case of the longitudinal quadrupole, near and far field directivity effects will in general appear, as illustrated in Figure 1 at right, showing a typical cardioid pattern.

F. Directivity and Near- and Far-field Effects

The general model given in (13) leads, obviously, to solutions with directivity. To recover standard directivity patterns from the solution in (15), one may assume sinusoidal variation of the coefficients $\Psi^{(q)}$ at angular frequency ω , or $\Psi^{(q)} = \hat{\Psi}^{(q)} e^{-j\omega t}$, for constants $\hat{\Psi}^{(q)}$, $q = 0, \dots$. In this case, the solution (15) may be written as $p(\mathbf{r}, t) = e^{-j\omega t} \hat{p}(\mathbf{r}, \omega)$, where

$$\hat{p}(\mathbf{r}, \omega) = \frac{1}{4\pi} \sum_{q=0}^{\infty} \hat{\Psi}^{(q)} \cdot^{(q)} \nabla^q \left(\frac{e^{j\omega r/c}}{r} \right). \quad (20)$$

For a given radius r and direction \mathbf{d} , one can write an expression for the normalised directivity of the source as

$$D(r, \mathbf{d}, \omega) = \frac{|\hat{p}(\mathbf{r}, \omega)|}{\max_{\mathbf{d}} |\hat{p}(\mathbf{r}, \omega)|}. \quad (21)$$

For monopole and dipole sources, directivity is independent of frequency ω . For higher order multipoles, near and far field effects will, in general, appear. See Figure 1, illustrating directivity patterns for a variety of source types.

G. Separable Decompositions of Source Terms

Except in the case of the monopole, the source term $f^{(q)}(\mathbf{r})$ is not separable according to the coordinates \mathbf{r} . Each individual term under the inner product in (14), however, is separable. Indeed, the entry $\Upsilon_{\gamma}^{(q)}$ of $\Upsilon^{(q)}$ with index γ has the form:

$$\Upsilon_{\gamma}^{(q)} = \left(\prod_{\nu=1}^3 \partial_{r_{\nu}}^{q_{\nu}} \right) \delta^{(3)}(\mathbf{r}) = \prod_{\nu=1}^3 \underbrace{\partial_{r_{\nu}}^{q_{\nu}} \delta^{(1)}(r_{\nu})}_{w_{\nu}^{(q_{\nu})}}. \quad (22)$$

Here, separability of the 3D Dirac delta function (6) has been used, and where q_{ν} , $\nu = 1, \dots, 3$ is the number of elements of γ which take on the value ν (and thus $\sum_{\nu=1}^3 q_{\nu} = q$). The separability property leads to simplifications when approximating such distributions over a grid, as 1D forms (indicated as $w_{\nu}^{(q_{\nu})}$, representing the q_{ν} th spatial derivative of a 1D Dirac delta function, in coordinate r_{ν}) may be approximated individually and then recombined.

IV. APPROXIMATIONS TO THE DIRAC DELTA FUNCTION AND ITS DERIVATIVES

FDTD methods for acoustics applications are normally defined over regular spatial grids which are often (but not always) chosen to be Cartesian. For point-like sources as described in Section III, a discrete representation is thus necessary.

Consider a spatial Cartesian grid, defined over grid indices $\mathbf{l} = [l_1, l_2, l_3] \in \mathbb{Z}^3$, corresponding to locations $\mathbf{x} = \mathbf{l}X$, where X is the grid spacing. An arbitrary source location \mathbf{x}_S may be represented uniquely with reference to the grid as

$$\mathbf{x}_S = (\mathbf{l}_S + \boldsymbol{\xi}_S) X, \quad (23)$$

where $\mathbf{l}_S \in \mathbb{Z}^3$, and where $\boldsymbol{\xi}_S = [\xi_{S,1}, \xi_{S,2}, \xi_{S,3}]$ satisfies $-\frac{1}{2} \leq \xi_{S,\nu} < \frac{1}{2}$, $\nu = 1, 2, 3$. Here, \mathbf{l}_S is the nearest rounded integer grid location to the source location, and $\boldsymbol{\xi}_S$ is the fractional remainder. In this section, we further assume $0 \leq \xi_{S,\nu} < \frac{1}{2}$, $\nu = 1, 2, 3$ without loss of generality.

A grid function $f = f_1$ may be constructed as an approximation to a continuously variable function $f(\mathbf{x})$, at locations $\mathbf{x}_1 = \mathbf{l}X$. A useful representation of such a grid function, when intended to approximate a localised distribution is

$$f_1 = \sum_{\mathbf{l}' \in \mathbb{B}} b_{\mathbf{l}'} \mathcal{I}_{\mathbf{l}-\mathbf{l}'}. \quad (24)$$

Here, $\mathbb{B} \in \mathbb{Z}^3$ represents the family of grid points over which the approximation is taken, relative to \mathbf{l}_S , and $b_{\mathbf{l}'}$, $\mathbf{l}' \in \mathbb{B}$ are the corresponding coefficients. The symbol $\mathcal{I}_{\mathbf{q}}$, for $\mathbf{q} \in \mathbb{Z}^3$ is the indicator function (or 3D Kronecker delta), taking the value 1 when $\mathbf{q} = \mathbf{0}$, and 0 otherwise.

For local approximations, there are various useful choices of the set \mathbb{B} . One choice is the cubic domain $\mathbb{B}_{\square,N}^{(3)}$, for integer N , which may be defined as a Cartesian product $\mathbb{B}_{\square,N}^{(3)} = \mathbb{B}_N^{(1)} \times \mathbb{B}_N^{(1)} \times \mathbb{B}_N^{(1)}$ of 1D domains $\mathbb{B}_N^{(1)}$, where

$$\mathbb{B}_N^{(1)} = [-\lfloor \frac{N-1}{2} \rfloor, \dots, \lfloor \frac{N}{2} \rfloor], \quad (25)$$

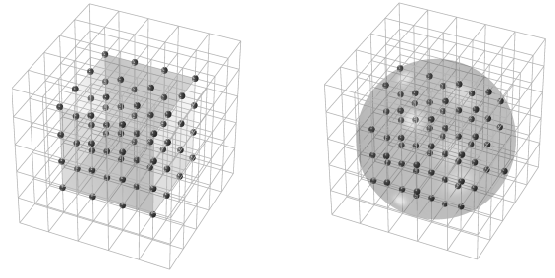


Fig. 2: Domains $\mathbb{B}_{\square,N}^{(3)}$ and $\mathbb{B}_{o,N}^{(3)}$, for $N = 4$.

and where $\lfloor \cdot \rfloor$ indicates a flooring operation. Another is the spherical distribution $\mathbb{B} = \mathbb{B}_{o,N}^{(3)}$, where

$$\mathbb{B}_{o,N}^{(3)} = \{\mathbf{l}' \in \mathbb{Z}^3 \mid \|\mathbf{l}' - \boldsymbol{\xi}_S\|_2 \leq (3/4\pi)^{1/3} N\}, \quad (26)$$

which is an excellent match in isotropic problems such as the wave equation (2). The additional factor of $(3/4\pi)^{1/3}$ above serves to equalise the computational cost of approximation over the two domains $\mathbb{B}_{\square,N}^{(3)}$ and $\mathbb{B} = \mathbb{B}_{o,N}^{(3)}$. See Figure 2 for an illustration of the two distributions.

A. Spatial Fourier Transforms

Because of the point-like nature of the source terms, approximations over a grid are best approached in the spatial Fourier transform domain. For a continuous function $f(\mathbf{r})$, the spatial Fourier transform $\hat{f}(\mathbf{k})$ is defined, in terms of wave vectors $\mathbf{k} = [k_1 \ k_2 \ k_3] \in \mathbb{R}^3$, as

$$\hat{f}(\mathbf{k}) = \iiint_{\mathbb{R}^3} f(\mathbf{r}) e^{-j\mathbf{k} \cdot \mathbf{r}} d\mathbf{r}. \quad (27)$$

In particular, for the source terms $f^{(q)}(\mathbf{r})$, as defined in (14), the spatial Fourier transforms $\hat{f}^{(q)}(\mathbf{k})$ follow as

$$\hat{f}^{(q)}(\mathbf{k}) = \boldsymbol{\Psi}^{(q)} \cdot (j\mathbf{k})^q, \quad (28)$$

where an inner product as defined in (68) has been used, and where $(j\mathbf{k})^q$ is a q th-order tensor, as defined in (69). See the Appendix.

In the case of grid functions f_1 , a discrete 3D spatial Fourier transform may be defined as

$$\hat{f}_{d,\mathbf{x}}(\mathbf{k}) = X^3 \sum_{\mathbf{l}' \in \mathbb{Z}^3} f_1 e^{-j\mathbf{k} \cdot \mathbf{l}X} \quad (29)$$

in terms of a discrete wave vector \mathbf{k} , defined over the cube-shaped region $\|\mathbf{k}\|_{\infty} \leq \pi/X$. Note that the definition in (29) above incorporates a factor of X^3 , for consistency with the continuous Fourier transform, as defined in (27). This transform is defined with respect to the absolute coordinates \mathbf{x} (and hence the subscript \mathbf{x} in $\hat{f}_{d,\mathbf{x}}(\mathbf{k})$).

Consider now a grid function f_1 defined with respect to a particular local approximation region \mathbb{B} , with associated coefficients b , as in (24). The discrete Fourier transform (29) may now be written as

$$\hat{f}_{d,\mathbf{x}}(\mathbf{k}) = X^3 \sum_{\mathbf{l}' \in \mathbb{B}} b_{\mathbf{l}'} e^{-j\mathbf{k} \cdot (\mathbf{l}' + \mathbf{l}_S)X}. \quad (30)$$

A shift to a Fourier transform \hat{f}_d defined over source-centered coordinates follows from a multiplication by a phase factor corresponding to a displacement of $\mathbf{x}_S = (\mathbf{l}_S + \boldsymbol{\xi}_S)X$:

$$\hat{f}_d(\mathbf{k}) = e^{j\mathbf{k} \cdot (\mathbf{l}_S + \boldsymbol{\xi}_S)X} \hat{f}_{d,\mathbf{x}} = X^3 \sum_{\mathbf{l}' \in \mathbb{B}} b_{\mathbf{l}'} e^{-j\mathbf{k} \cdot (\mathbf{l}' - \boldsymbol{\xi}_S)X}. \quad (31)$$

B. Consistency of Approximations and Constraints

Consider now the q th-order source term $f^{(q)}$, as defined in (14), and an approximation over a region \mathbb{B} , with coefficients $b_{\mathbf{l}'}^{(q)} = \tilde{b}_{\mathbf{l}'}^{(q)} / X^{3+q}$, which may be written as

$$f_1^{(q)} = \frac{1}{X^{3+q}} \sum_{\mathbf{l}' \in \mathbb{B}} \tilde{b}_{\mathbf{l}'}^{(q)} \mathcal{I}_{\mathbf{l}-\mathbf{l}_S-\mathbf{l}'}. \quad (32)$$

The source-centred discrete Fourier transform (31) is then

$$\hat{f}_d^{(q)} = \frac{1}{X^q} \sum_{\mathbf{l}' \in \mathbb{B}} \tilde{b}_{\mathbf{l}'}^{(q)} e^{-j\mathbf{k} \cdot (\mathbf{l}' - \boldsymbol{\xi}_S)X}. \quad (33)$$

Expanding this expression in Taylor series about $\mathbf{k} = \mathbf{0}$ gives

$$\hat{f}_d^{(q)} = \sum_{m=0}^{\infty} \frac{X^{m-q}}{m!} \sum_{\mathbf{l}' \in \mathbb{B}} \tilde{b}_{\mathbf{l}'}^{(q)} (-j\mathbf{k} \cdot (\mathbf{l}' - \boldsymbol{\xi}_S))^m. \quad (34)$$

By association with the Fourier transform of the continuous operator $f^{(q)}$, from (28), it is apparent that, for consistency of the approximation $\hat{f}_1^{(q)}$ with $f^{(q)}$, it must follow that the term in (34) with $m = q$ must satisfy

$$\frac{1}{q!} \sum_{\mathbf{l}' \in \mathbb{B}} \tilde{b}_{\mathbf{l}'}^{(q)} (-j\mathbf{k} \cdot (\mathbf{l}' - \boldsymbol{\xi}_S))^q = \boldsymbol{\Psi}^{(q)} \cdot (j\mathbf{k})^q. \quad (35)$$

Furthermore, for $q \geq 1$, all terms of lower order must vanish, for consistency with the transform (28), which only contains terms of order q in \mathbf{k} , and no lower order terms. In other words,

$$\sum_{\mathbf{l}' \in \mathbb{B}} \tilde{b}_{\mathbf{l}'}^{(q)} (-j\mathbf{k} \cdot (\mathbf{l}' - \boldsymbol{\xi}_S))^m = 0, \quad m = 0, \dots, q-1. \quad (36)$$

The conditions (35) and (36) above depend explicitly on the fractional remainder $\boldsymbol{\xi}_S$. By employing (36) recursively, and making use of the identity (70) (see the Appendix), one may arrive at the following set of conditions:

$$\sum_{\mathbf{l}' \in \mathbb{B}} \tilde{b}_{\mathbf{l}'}^{(q)} (\mathbf{l}')^q = (-1)^q q! \boldsymbol{\Psi}^{(q)} \quad (37)$$

and, for $q \geq 1$,

$$\sum_{\mathbf{l}' \in \mathbb{B}} \tilde{b}_{\mathbf{l}'}^{(q)} (\mathbf{l}')^m = 0, \quad m = 0, \dots, q-1. \quad (38)$$

These conditions, which are independent of the remainder $\boldsymbol{\xi}_S$, form a set of $(q+3)!/6q!$ affine constraints on the coefficients \tilde{b} , after taking into account symmetry of the tensor $\boldsymbol{\Psi}^{(q)}$. Such conditions enforce only consistency of the discrete approximations with the underlying continuous functions—it is possible to go further to enforce so-called moment conditions [29], [33], at the expense of a reduced parameter space available for optimisation over the full range of wavenumbers. Note also that terms in (34) with order $m > q$ do not vanish identically, representing errors in the high wavenumber range—but such terms are accompanied by increasing powers of X , the grid spacing, and thus vanish in the limit as X becomes small.

C. Separable Approximations

Analytic simplifications are possible if the function to be approximated and corresponding domain \mathbb{B} are separable. A separable domain $\mathbb{B}_{\square,N}^{(3)}$ has been defined in (25), and, as noted in Section III-G, any source term $f^{(q)}$ may be decomposed into a weighted sum of terms of the form (22), each of which is separable according to the coordinates \mathbf{r} . For each separable term $\Upsilon_{\gamma}^{(q)}$ in $f^{(q)}$, one may then design 1D approximants $w_{\nu,l_{\nu}}^{(q_{\nu})}$, defined over the domains $\mathbf{l}_{\nu} \in \mathbb{B}_N^{(1)}$ as

$$w_{\nu,l_{\nu}}^{(q_{\nu})} = \sum_{\mathbf{l}'_{\nu} \in \mathbb{B}_N^{(1)}} b_{\nu,l_{\nu}}^{(q)} \mathcal{I}_{\mathbf{l}_{\nu}-\mathbf{l}_{S,\nu}-\mathbf{l}'_{\nu}}, \quad (39)$$

such that the grid function $\Upsilon_{\gamma,\mathbf{l}}^{(q)}$ approximates $\Upsilon_{\gamma}^{(q)}$ as

$$\Upsilon_{\gamma,\mathbf{l}}^{(q)} = \prod_{\nu=1}^3 w_{\nu,l_{\nu}}^{(q_{\nu})}. \quad (40)$$

For the sake of notational simplicity, it is useful to introduce the symbol $w^{(g)} = (d/d\sigma)^g \delta^{(1)}(\sigma)$, representing the g th derivative of a 1D Dirac delta function, for $g \geq 0$, and regardless of the spatial coordinate (a dummy coordinate σ has been employed above). The associated 1D spatial Fourier transform $\hat{w}^{(g)}$ may be written as

$$\hat{w}^{(g)} = \int_{-\infty}^{\infty} (d/d\sigma)^g \delta^{(1)}(\sigma) e^{-jk\sigma} d\sigma = (-jk)^g \quad (41)$$

in terms of a scalar wavenumber k . 1D approximants to $w^{(g)}$ may be written as $w_l^{(g)}$, for $l \in \mathbb{Z}$, and expressed explicitly in terms of coefficients $c_{\mathbf{l}'}^{(g)}$, $\mathbf{l}' \in \mathbb{B}_N^{(1)}$ as

$$w_l^{(g)} = \sum_{\mathbf{l}' \in \mathbb{B}_N^{(1)}} c_{\mathbf{l}'}^{(g)} \mathcal{I}_{\mathbf{l}-\mathbf{l}_S-\mathbf{l}'}, \quad (42)$$

and will be associated with a scalar nearest-neighbour grid location \mathbf{l}_S , and a scalar fractional grid distance $\boldsymbol{\xi}_S$, assumed here, by symmetry, to lie over the range $0 \leq \boldsymbol{\xi}_S < \frac{1}{2}$. For such 1D approximants, it is useful again to introduce scaled coefficients as $\tilde{c}_{\mathbf{l}'}^{(g)} = X^{1+g} c_{\mathbf{l}'}^{(g)}$. Taylor expansion of the 1D Fourier transform of $w_l^{(g)}$, defined as

$$\hat{w}_d^{(g)} = \frac{1}{X^g} \sum_{\mathbf{l}' \in \mathbb{B}_N^{(1)}} \tilde{c}_{\mathbf{l}'}^{(g)} e^{-j\mathbf{k} \cdot (\mathbf{l}' - \boldsymbol{\xi}_S)X}, \quad (43)$$

again phase shifted corresponding to a displacement of $\mathbf{l}_S + \boldsymbol{\xi}_S$, leads to the following consistency conditions:

$$\sum_{\mathbf{l}' \in \mathbb{B}_N^{(1)}} \tilde{c}_{\mathbf{l}'}^{(g)} (\mathbf{l}')^g = (-1)^g g! \quad (44)$$

and, for $g \geq 1$,

$$\sum_{\mathbf{l}' \in \mathbb{B}_N^{(1)}} \tilde{c}_{\mathbf{l}'}^{(m)} (\mathbf{l}')^m = 0, \quad m = 0, \dots, g-1. \quad (45)$$

D. Nearest-Neighbour and Trilinear Approximations

The most basic type of approximation is that of nearest-neighbour type—the approximation point is taken to be the nearest grid location to the source location. In this case, separable approximations may be defined recursively, through repeated application of difference operators to a single Kronecker delta function centered at the grid location l_S , as

$$w_l^{(g)} = D_-^{g-} D_+^{g+} \mathcal{I}_{l-l_S}, \quad (46)$$

where D_- and D_+ are defined as

$$D_- \mathcal{I}_j = \frac{1}{X} (\mathcal{I}_j - \mathcal{I}_{j+1}) \quad D_+ \mathcal{I}_j = \frac{1}{X} (\mathcal{I}_{j-1} - \mathcal{I}_j), \quad (47)$$

and where $g_- = \lfloor g/2 \rfloor$ and $g_+ = \lfloor (g+1)/2 \rfloor$ indicate powers of D_- and D_+ , respectively. This definition leads to a series of approximations defined over $\mathbb{B}_{g+1}^{(1)}$, minimal for a given order of differentiation g ; it is easily verified that the 1D consistency conditions (44) and (45) are satisfied automatically in this case.

A better approximation, using the fractional remainder ξ_S , may be obtained from the nearest-neighbour form through two-point averaging or linear interpolation, or as

$$w_l^{(g)} = M_{\xi_S}^{(g)} D_-^{g-} D_+^{g+} \mathcal{I}_{l-l_S}. \quad (48)$$

In this case, the averaging operator $M_{\xi_S}^{(g)}$ is defined, in terms of its action on a Kronecker delta function \mathcal{I}_j , as

$$M_{\xi_S}^{(g)} \mathcal{I}_j = \begin{cases} (1 - \xi_S) \mathcal{I}_j + \xi_S \mathcal{I}_{j-1}, & g \text{ even} \\ (\frac{1}{2} + \xi_S) \mathcal{I}_j + (\frac{1}{2} - \xi_S) \mathcal{I}_{j+1}, & g \text{ odd} \end{cases}. \quad (49)$$

Such 1D linear approximants, when combined into a 3D approximant lead to a standard trilinear approximant. It is again easily verified that the 1D consistency conditions (44) and (45) are satisfied automatically in this case. See Figure 3, illustrating such nearest neighbour and linear approximants, for various orders g .

E. Optimised Separable Approximations

The nearest-neighbour and trilinear approximations may be derived explicitly. Another approach is to optimise directly in the Fourier domain against the transform of the multipole distribution, from (28). To this end, and defining a normalised wavenumber $\tilde{k} = Xk$, one may define a least-squares error measure in the wavenumber domain as

$$\begin{aligned} E_{\zeta}^{(g)} &= X^g \int_{-\pi\zeta}^{\pi\zeta} |\hat{w}_d^{(g)}(\tilde{k}) - \hat{w}^{(g)}(\tilde{k})|^2 d\tilde{k} \\ &= \int_{-\pi\zeta}^{\pi\zeta} \left| \sum_{l' \in \mathbb{B}_N^{(1)}} \tilde{c}_{l'}^{(g)} e^{-j\tilde{k}(l_S - \xi_S)} - (j\tilde{k})^g \right|^2 d\tilde{k}. \end{aligned} \quad (50)$$

Here, the parameter ζ , with $0 < \zeta \leq 1$ allows for the selection of a wavenumber range for the optimisation, and constitutes an additional degree of control over the resulting approximant—which is useful when used in the finite difference setting, where it may be used in conjunction with knowledge about the dispersive properties of a given scheme. This will be described further in Section V.

In this case, the consistency conditions (44) and (45) are not satisfied automatically, and form an additional $g+1$ affine

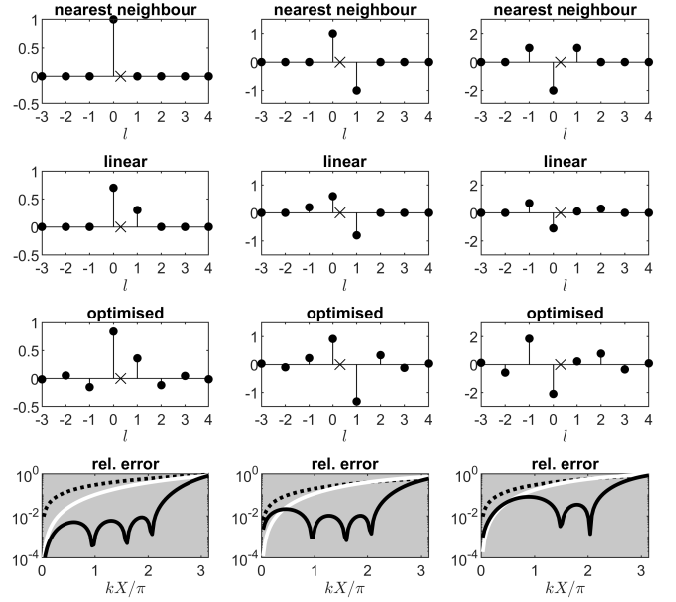


Fig. 3: Discrete approximations to the g th derivative of the 1D Dirac delta function, about a given fractional grid location (indicated here by a cross), where g is as indicated. In each case, a simple nearest-neighbour approximation is shown (top row), as well as a linear approximant (second row) and an optimised approximant (third row), using $N = 8$, and a relative bandwidth of $\zeta = 0.7$. In the bottom row, the relative error $|\hat{w}_d^{(g)} - \hat{w}^{(g)}|/|\hat{w}^{(g)}|$ is shown as a function of normalised wavenumber kX/π for the nearest-neighbour (dotted), linear (white) and optimised (black) approximants.

constraints. Using the error measure (51), a constrained least-squares optimisation problem results. See Figure 3, illustrating a typical optimised approximant. Upon recombination of the 1D approximants, a 3D approximant results over the cube-shaped wave vector region $\mathbf{k} \in \mathbb{U}_{\square, \zeta}$, defined as

$$\mathbb{U}_{\square, \zeta} = \{\mathbf{k} \in \mathbb{R}^3 \mid \|\mathbf{k}\|_{\infty} \leq \pi\zeta/X\}. \quad (51)$$

The region $\mathbb{U}_{\square, \zeta}$ is shown in Figure 4 at left.

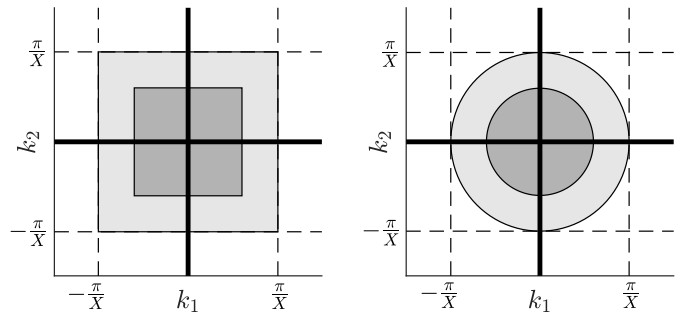


Fig. 4: Cross-sections, in the k_1, k_2 plane, of the cube-shaped wave vector region $\mathbb{U}_{\square, \zeta}$ (at left) and the spherical region $\mathbb{U}_{\circ, \zeta}$ (at right), for $\zeta = 1$ (light grey) and $\zeta = 0.6$ (grey).

F. Nonseparable Approximations

Loosening the requirement of separability leads to more general approximation strategies. In this case, a source distribution f may be approximated in its entirety, without the requirement of an additive decomposition into separable components. In addition, for optimisation purposes, one may introduce the more natural wave-vector range $\mathbb{U}_{\circ, \zeta}$, defined as

$$\mathbb{U}_{\circ, \zeta} = \{\mathbf{k} \in \mathbb{R}^3 \mid \|\mathbf{k}\|_2 \leq \pi\zeta/X\}. \quad (52)$$

The wave-vector range $\mathbb{U}_{o,\zeta}$ is spherical, and parameterised by ζ , with $0 < \zeta \leq 1$. The region $\mathbb{U}_{o,\zeta}$ is shown in Figure 4 at right.

Consider a general approximant $f = f_1$ as defined in (24) intended to approximate a distribution $f(\mathbf{r})$, for a set of coefficients $b_{\mathbf{l}}$, $\mathbf{l} \in \mathbb{B}$. An optimal constrained least-squares approximation over the wave-vector range $\mathbb{U}_{o,\zeta}$ follows from the minimisation of the error function

$$E_\zeta = \iiint_{\mathbb{U}_{o,\zeta}} |\hat{f}_d - \hat{f}|^2 d\mathbf{k} \quad (53)$$

with respect to the coefficients $b_{\mathbf{l}}$, $\mathbf{l} \in \mathbb{B}$. As the approximant $f = f_1$ is linear in the coefficients $b_{\mathbf{l}}$, a linear system results, subject to the consistency constraints (35) and (36). In this article, for such nonseparable approximants, $\mathbb{B} = \mathbb{B}_{o,N}$ is used.

V. FINITE DIFFERENCE TIME DOMAIN METHODS

Finite difference time domain methods represent what is perhaps the simplest approach to volumetric time domain modeling in the context of room acoustics. The spatial domain under study is represented over a uniform grid, and time stepping is performed at a fixed rate. FDTD basics are covered in many texts [34], [35], and a great variety of schemes have been proposed for 3D acoustics applications [36]. The representations of point-like source terms as presented here are relatively independent of the particular choice of scheme. Although the best known, and by far the simplest is the so-called seven-point scheme, described below, in the interest of examining the behaviour of the various source term approximations, particularly in the high frequency range, a higher order accurate scheme (fourth-order in time and space) will be employed here. The source term approximations presented in this article can equally be used with simpler methods such as the seven-point scheme.

The spatial Cartesian grid in 3D has already been defined at the beginning of Section IV. A grid function p_1^n represents an approximation to a continuously variable function $p(\mathbf{x}, t)$, at locations $\mathbf{x} = \mathbf{l}X$ and at times $t = nT$, where here, X is the grid spacing, and T is the time step (and $F_s = 1/T$ is the associated sample rate).

The class of explicit two-step FDTD methods for the wave equation (2) may be written as

$$p_1^{n+1} - 2p_1^n + p_1^{n-1} - \lambda^2 L p_1^n = 0, \quad (54)$$

where the operator L is a discrete approximation to the Laplacian, scaled by X^2 , and is defined, in general, as

$$L p_1^n = \sum_{\mathbf{l} \in \mathbb{Q}} g_{\mathbf{l}} (p_{1+\mathbf{l}}^n - p_1^n). \quad (55)$$

Here, the set $\mathbb{Q} \in \mathbb{Z}^3 \setminus \mathbf{0}$ represents the stencil of points around the operating location of the scheme from which neighbouring values are drawn, and the scalars $g_{\mathbf{l}}$ are the associated scheme coefficients. The dimensionless parameter $\lambda = cT/X$ is often referred to as the Courant number for the scheme [34].

There is a wide variety of schemes, each characterised by a particular choice of stencil \mathbb{Q} and associated coefficients $g_{\mathbf{l}}$ —see, e.g., [37] for a catalogue of options. In all cases of interest, the scheme stencil and coefficients exhibit symmetry

with respect to the three coordinate directions: if $\mathbf{l} \in \mathbb{Q}$, with associated coefficient $g_{\mathbf{l}}$ then any permutation $\tilde{\mathbf{l}}$ of \mathbf{l} , under possible changes in sign, is also in \mathbb{Q} , and $g_{\tilde{\mathbf{l}}} = g_{\mathbf{l}}$. For consistency with the 3D Laplacian, the coefficients must satisfy $\sum_{\mathbf{l} \in \mathbb{Q}} g_{\mathbf{l}} |\mathbf{l}|^2 = 6$.

The basic Laplacian approximation defined by

$$\mathbb{Q} = \{\mathbf{q} \in \mathbb{Z}^3 \setminus \mathbf{0} \mid \|\mathbf{q}\|_1 = 1\} \quad g_{[1\ 0\ 0]} = 1 \quad (56)$$

is a popular choice, leading, when employed in (54), to the so-called seven-point scheme, the simplest possible scheme for the 3D wave equation; it is stable under the condition $\lambda \leq 1/\sqrt{3}$. Another more elaborate scheme [37], with fourth-order accuracy in space and time is described by

$$\mathbb{Q} = \{[1\ 0\ 0], [1\ 1\ 0], [2\ 0\ 0], [1\ 1\ 1], [2\ 1\ 0]\}$$

$$\begin{aligned} g_{[1\ 0\ 0]} &= \frac{2}{15} + \frac{\lambda^2}{9} & g_{[1\ 1\ 0]} &= \frac{8}{5} - \frac{8\lambda^2}{9} & g_{[2\ 0\ 0]} &= \frac{1}{5} - \frac{\lambda^2}{9} \\ g_{[1\ 1\ 1]} &= -\frac{4}{15} + \frac{\lambda^2}{3} & g_{[2\ 1\ 0]} &= -\frac{2}{3} + \frac{5\lambda^2}{9}. \end{aligned} \quad (57)$$

In this case, the scheme (54) is stable under the condition $0.516 < \lambda \leq 0.897$.

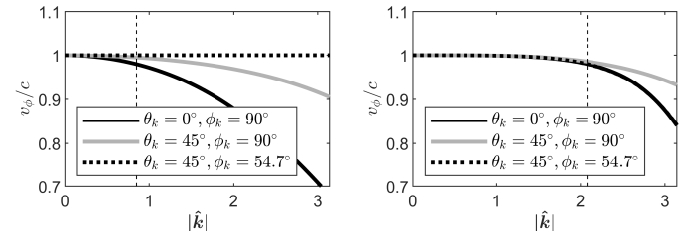


Fig. 5: Relative numerical phase velocities, as a function of normalised wavenumber \tilde{k} , for various angles of propagation (as indicated), chosen to indicate best and worst cases. Left: for the simple scheme with coefficients as defined in (56), and right: for the fourth-order accurate scheme with coefficients as given in (57). The 2% error threshold is indicated as a dashed line.

A. Numerical Dispersion

The dispersive behaviour of any such scheme may be characterised in terms of a dispersion relation $\omega = \omega(\mathbf{k})$, which is obtained by examining harmonic solutions of the form $p_1^n = e^{j(-\omega nT + \mathbf{k} \cdot \mathbf{l}X)}$, for wave vectors over the discrete range $\|\mathbf{k}\|_\infty \leq \pi/X$. The numerical phase velocity $v_{\text{phase}}(\mathbf{k}) = \omega/|\mathbf{k}|$ is generally dependent on the wave vector, and thus direction dependent, and, in particular, is not equal to c , the phase velocity for plane-wave solutions to the wave equation. It is useful to show comparisons of the relative phase velocity $v_{\text{phase}}(\mathbf{k})/c$ for the two aforementioned schemes operating at their respective stability limits, as a function of normalised wave vector $\tilde{\mathbf{k}} = X\mathbf{k}$, where

$$\tilde{\mathbf{k}} = \tilde{k} [\sin(\phi_k) \cos(\theta_k) \quad \sin(\phi_k) \sin(\theta_k) \quad \cos(\phi_k)]. \quad (58)$$

Here, \tilde{k} is the normalised wavenumber, and θ_k and ϕ_k are the azimuth/inclination angle pair defining the direction of propagation of a plane wave. See Figure 5, showing the numerical phase velocities for the two schemes described in this article. In particular, note that the phase velocity exhibits a high degree of variation for the simple scheme defined by coefficient choice (56), reaching an error of 2% at $\tilde{k} = 0.27\pi$

whereas the variation is greatly decreased in the case of the fourth-order scheme given by the choice (57), and the 2% threshold is reached at $\tilde{k} = 0.65\pi$.

For the remainder of this article, except when indicated otherwise, the scheme defined by (57) will be used, at the maximal Courant number $\lambda = 0.897$.

B. Source Terms and Input Filtering

The dispersion analysis presented above neglects the presence of the source term. A useful approach to such an analysis, including sources, is to make use of so-called modified equation techniques [38], [39]. Only a very abbreviated treatment is presented here—see [37] for an in-depth presentation. First assume that the grid function p_1^n represents samples of an underlying continuous function $p^\dagger(\mathbf{x}, t)$, at $\mathbf{x} = \mathbf{l}X$ and $t = nT$. Expanding in Taylor series leads, in the case of the simple source-free scheme (54) defined by the coefficients (56), and using constant λ , to the modified equation

$$\left(\frac{1}{c^2}\partial_t^2 - \Delta\right)p^\dagger = O(T^2). \quad (59)$$

The modified equation differs from the wave equation by a term with $O(T^2)$ in the time step T , and the solution is a second-order accurate approximation. In the case of the fourth-order scheme, of coefficients given by (57), the corresponding modified equation is

$$\underbrace{\left(1 + \frac{T^2}{12}(\partial_t^2 + c^2\Delta)\right)}_G \left(\frac{1}{c^2}\partial_t^2 - \Delta\right)p^\dagger = O(T^4), \quad (60)$$

which differs from the wave equation by a term in $O(T^4)$, leading to a fourth-order accurate solution. It also includes an additional operator, written above as G , which approximates the identity to second order in T . It is this additional operation which must be included in a full model of the inhomogeneous wave equation in (13). Indeed, consider the scheme

$$p_1^{n+1} - 2p_1^n + p_1^{n-1} - \lambda^2 L p_1^n - T^2 \bar{f}_1^n = 0, \quad (61)$$

where \bar{f} is some approximation to Gf , accurate to at least second order in T , and thus $\bar{f} = Gf + O(T^2)$. Again expanding in Taylor series,

$$G \left(\left(\frac{1}{c^2} \partial_t^2 - \Delta \right) p^\dagger - f \right) = O(T^4) \quad (62)$$

and, because $G = O(1)$, fourth-order accuracy follows; due to the nature of the operator G , one would expect such a correction to be of importance in the high frequency range. The operator G , consisting of both spatial and temporal differential operators, can be employed a priori to the source term f , if it is of a known form. A further simplification is to use $G \approx 1 + \frac{T^2}{6}\partial_t^2$, eliminating the need for spatial differentiation of the source term, but reducing accuracy to second order. This approach is taken in the remainder of this article. If the time dependence of the source term is not known a priori, then a good further discrete-time approximation is

$$\bar{f}_1^n = f_1^n + \frac{1}{6} (f_1^{n+1} - 2f_1^n + f_1^{n-1}), \quad (63)$$

which may be used as pre-filtering applied to the temporally-varying factors in the sampled time series f_1^n , and an illustrative example appears in Section VI-A.

C. Output Interpolation and Receivers

The problem of pointwise receiver design is dual to that presented here for a source, and is not presented here in detail. Drawing a value for the pressure p from the solution to (2) at a location \mathbf{x} may be written, formally, through the use of a Dirac delta function, as

$$p_{\text{out}}(t) = p(\mathbf{x}, t) = \iiint_{\mathbb{D}} \delta^{(3)}(\mathbf{x}' - \mathbf{x}) p(\mathbf{x}', t) d\mathbf{x}'. \quad (64)$$

By reciprocity, all of the approximant types presented in Section IV may equally well be used as interpolants in order to draw output from a particular location on the grid; in this article, only omnidirectional output will be used. Consider a receiver located at absolute coordinates \mathbf{x}_R . As in the case of the source, the receiver location may be written uniquely in terms of a nearest grid location \mathbf{l}_R and fractional index $\boldsymbol{\xi}_R$ as $\mathbf{x}_R = X(\mathbf{l}_R + \boldsymbol{\xi}_R)$. Employing the procedures in Section IV, with \mathbf{l}_R and $\boldsymbol{\xi}_R$ in place of \mathbf{l}_S and $\boldsymbol{\xi}_S$, for an interpolant defined over \mathbb{B} , with coefficients $b_{\mathbf{l}'}$, $\mathbf{l}' \in \mathbb{B}$, omnidirectional output p_R^n at the receiver may be drawn as

$$p_R^n = X^3 \sum_{\mathbf{l}' \in \mathbb{B}} b_{\mathbf{l}'} p_{\mathbf{l}-\mathbf{l}'}^n. \quad (65)$$

Note the factor X^3 , which follows from consistency with the expression in the continuous case from (64), with $\mathbf{x} = \mathbf{x}_R$.

VI. NUMERICAL RESULTS

It is obviously difficult, given the large number of design parameters, to illustrate the complete behaviour of these families of approximants. Some features have been selected here in order to illustrate basic properties of these methods—these will be examined with regard to comparisons between exact and numerically-computed transients both in the time domain, as well as in terms of numerical source directivity for steady sinusoidal forcing. A basic example of the use of such approximants in a dynamic setting is also presented here.

For transient responses, forcing functions of bandlimited Gaussian type will be used:

$$\psi(t) = e^{-\sigma(t-t_0)^2} * \frac{\sin(\zeta_{\text{in}}\pi t/T)}{\pi t}. \quad (66)$$

Here, ψ represents any one component of the multipole tensors $\Psi^{(p)}$, $\sigma > 0$ is a parameter determining the width of the pulse, and t_0 is a time delay chosen in all cases such that the starting value $\psi(0)$ is suitably small. $*$ represents the temporal convolution operation, and $0 < \zeta_{\text{in}} \leq 1$ is the normalised bandwidth.

For directivity plots, a ramped sinusoid of the form

$$\psi(t) = W(t/T_0) e^{2\pi j f_{\text{in}} t} \quad (67)$$

is used, with frequency f_{in} , in Hz, and where a ramp function W is used to avoid transient artefacts. In this work, the ramp function is chosen as $W(\gamma) = \sin^2(\pi\gamma/2)$ for $\gamma \leq 1$, and $W(\gamma) = 1$ for $\gamma > 1$; for directivity plots, the ramp duration

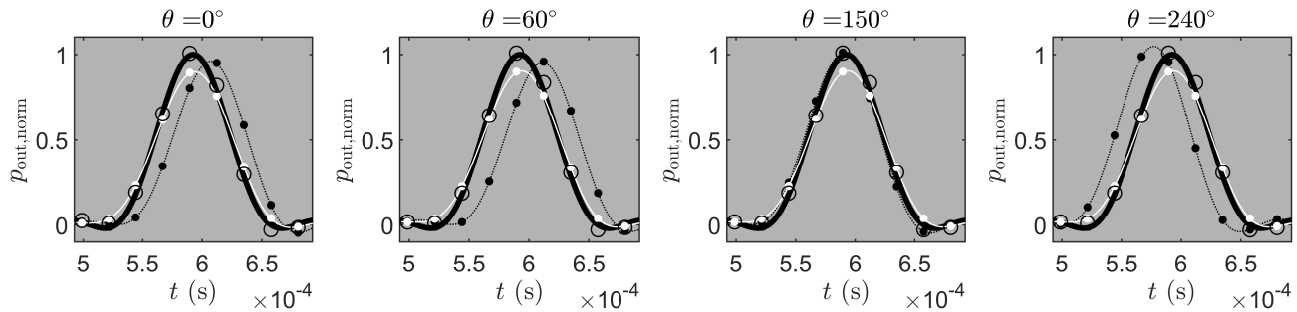


Fig. 6: Responses to a Gaussian pulse at a fixed distance from the source, at directions of angles θ as indicated. Solid black: exact solution. Dotted: nearest-neighbour approximation. White: Trilinear approximation. Circles: 12th-order separable approximation. Calculated values (shown as dots) are interpolated in time for better visibility. Simulation parameters are as given at the beginning of Section VI-A.

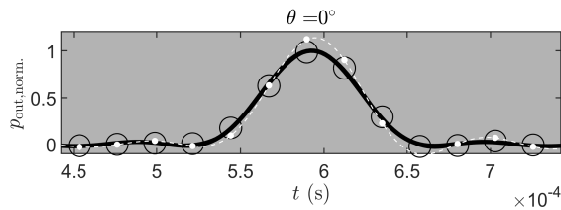


Fig. 7: Simulated response using prefiltering stage (63) (circles), and without prefiltering (dashed white). The exact solution is shown in black. Simulation parameters are as in the caption to Figure 6, and a 12th-order optimised separable approximant is used.

is chosen as $T_0 = 0.725$ ms. For the special case of moving sources, as described in Section VI-D, the real part of the signal (67) is used, with a ramp duration of two periods of the signal.

All solutions are generated using scheme (61) with coefficients (57), over a cube-shaped region, and where $c = 344$ m/s and running at 44.1 kHz, except in the case of moving sources in Section VI-D, where coefficients (56) are used. The input signals (66) and (67) are sampled at this rate. Simulations are halted before reflections from the domain boundaries reach the receiver locations. All solutions are read using a 12th-order separable optimised omnidirectional receiver—see Sections IV-E and V-C.

A. Monopole Responses

As a basic result, consider the transient response to a monopole excitation, where $\Psi^{(0)} = \psi(t)$, as per (66), with $\sigma = 8 \times 10^8$ and $\zeta_{\text{in}} = 0.6$. The scheme is excited at a location with $\xi_S = [-\frac{1}{2}, -\frac{1}{2}, -\frac{1}{2}]$, and a nearest-neighbour, trilinear and 12th-order separable approximant, optimised with $\zeta = 0.7$, are used. The solution is read at distances $r = 0.13$ m, for $\phi = \pi/2$ and a variety of azimuth angles θ . See Figure 6, showing numerical results compared with the exact solution, as given in (15). The basic expected result is that the nearest-neighbour approximant exhibits a large phase error, seen here as a time shift, to a degree which is highly dependent on the direction of propagation; the trilinear response is properly centered, but exhibits a large amplitude error. These effects are mitigated considerably for the optimised source approximant.

In the simulations presented above, the prefiltering stage described in Section V-B has been applied to $\Psi^{(0)}$. To demonstrate the effect of such prefiltering, consider the same

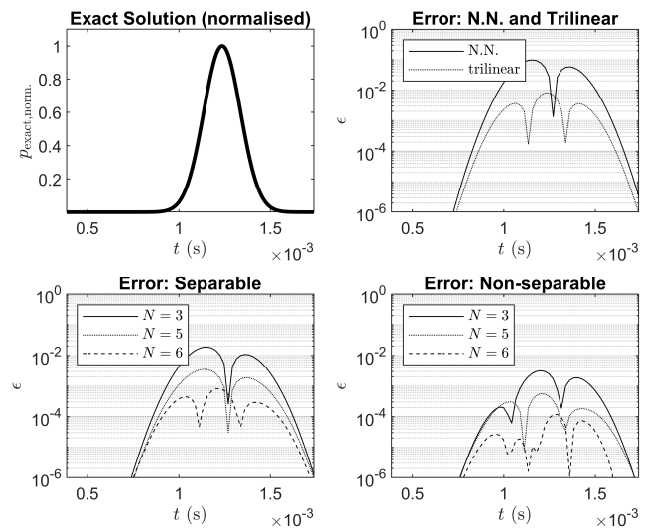


Fig. 8: Top left: normalised exact solution, for the wave equation excited by a monopole with Gaussian source strength at a distance $r = 0.13$ m. Normalised error sequences $\epsilon^n = (p_{\text{out}}^n - p_{\text{exact}}^n) / \max(|p_{\text{exact}}^n|)$ are shown for nearest-neighbour and trilinear approximants (top right), optimised separable approximants, of order N as indicated (bottom left) and optimised nonseparable approximants (bottom right). For optimised approximants, the relative bandwidth $\zeta = 0.5$ is used.

simulation as described above, in the case of the high-order separable approximant to the monopole. See Figure 7, showing the inaccuracy in both amplitude and phase when the prefiltering is not applied. Prefiltering will be applied in the remaining numerical examples presented in this article.

In the interest of examining the effect of the order of separable and non-separable source approximants on solution accuracy, consider the same simulation setting, but with a much wider pulse of the form (66), with $\sigma = 5 \times 10^7$ and $\zeta_{\text{in}} = 1$. Here, a direction of $\theta = 0^\circ$ is used, and with $\xi_S = [-\frac{1}{2}, -\frac{1}{2}, -\frac{1}{2}]$. See Figure 8, illustrating the error in the computed waveforms. Error is decreased by a order of magnitude for the trilinear approximant relative to that of the nearest-neighbour approximant. For the case of separable approximants, further reductions in error are shown for the cases $N = 3$, $N = 5$ and $N = 6$. For the nonseparable approximant, and for the same orders N (and thus of the same computational cost as the separable approximant), error is reduced by approximately an order of magnitude over the

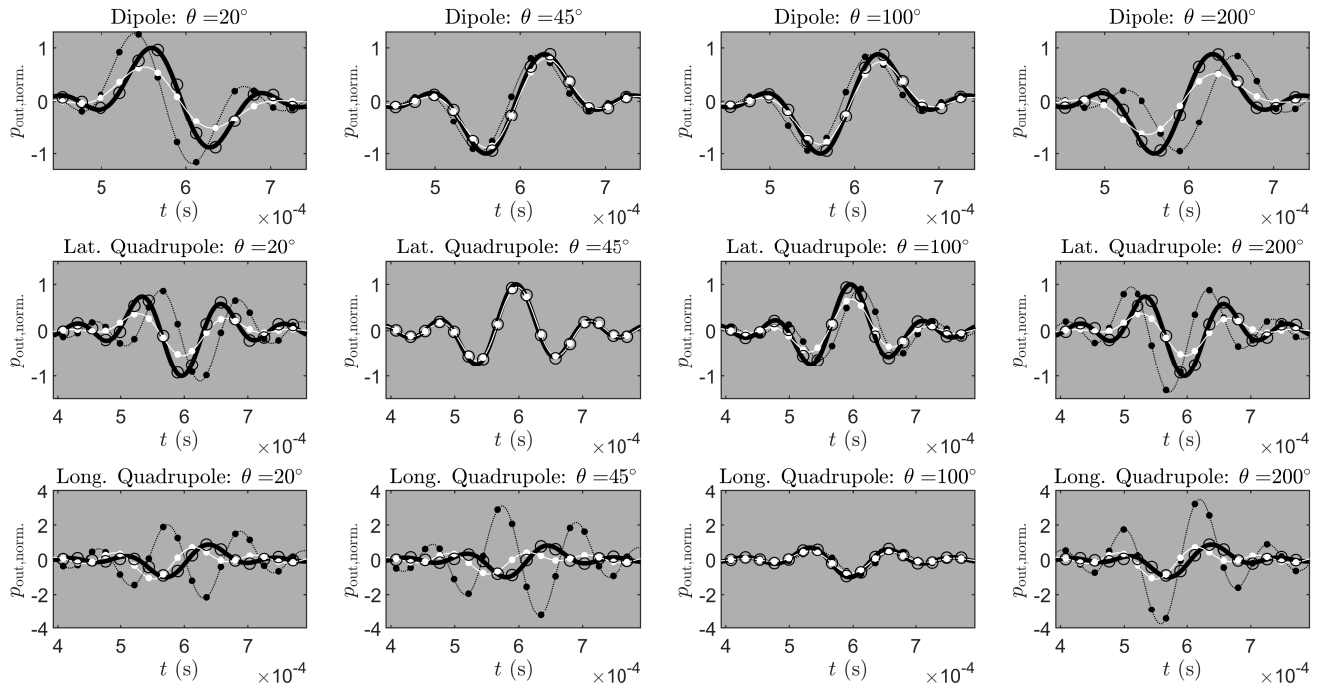


Fig. 9: Responses to a Gaussian pulse at a fixed distance from the source, at directions of angles θ as indicated, for a dipole, with $[\phi_D, \theta_D] = [\pi/2, 5\pi/3]$ in the top row, for a lateral quadrupole with $[\phi_Q, \theta_Q] = [\pi/2, \pi/6]$ and $[\hat{\phi}_Q, \hat{\theta}_Q] = [\pi/2, 5\pi/3]$ in the middle row, and for a longitudinal quadrupole with $[\phi_Q, \theta_Q] = [\pi/2, \pi/2]$ and $[\hat{\phi}_Q, \hat{\theta}_Q] = [\pi/2, \pi/2]$ in the bottom row. Solid black: exact solution. Dotted: nearest-neighbour approximation. White: Trilinear approximation. Circles: separable approximation. Calculated values (shown as dots) are interpolated in time for better visibility. Simulation parameters are as given at the beginning of Section VI-B.

same number of grid points as the separable approximant.

B. Higher-order Multipoles: Transient Responses

As might be expected, the accuracy of computed solutions degrades with the order of the multipole source term to be simulated. This is particularly true of nearest-neighbour and trilinear approximants, which are unable to resolve sharp pulses, as is evident from the simulation results presented for the dipole, lateral quadrupole and longitudinal quadrupole in Figure 9. In this case, the input function is as given in (66), with $\sigma = 8 \times 10^8$, and with $\zeta_{\text{in}} = 0.5$, and is used as the amplitude $-F$ in the case of the dipole and as $\psi^{(2)}$ for the quadrupoles. The solution is read at distances $r = 0.13$ m, for $\phi = 0$ and a variety of azimuth angles θ , as indicated, with a uniform fractional grid index of $\xi_S = [\frac{1}{2}, \frac{1}{2}, \frac{1}{2}]$. Of particular interest is the case of the longitudinal quadrupole, where the nearest-neighbour approximant fails dramatically; the optimised interpolants, which are of separable type and order $N = 8$, and optimised with $\zeta = 0.6$, track the exact solution very closely.

C. Higher-order Multipoles: Directivity

It is also useful to examine the directivity of such approximations, particularly in the high frequency range. In the low-frequency limit, all approximants presented here will have the correct directivity pattern, from the consistency constraints presented in Section IV-B. In Figure 10, directivity plots are presented in the case of the dipole, lateral quadrupole and longitudinal quadrupole, at $f_{\text{in}} = 5$ kHz and $f_{\text{in}} = 10$ kHz, and for a fractional grid index of $\xi_S = [0, 0, -\frac{1}{2}]$. An input signal of the form (67) is used to drive the multipole amplitude

($-F$ for the dipole, and $\psi^{(2)}$ for the quadrupoles). At these frequencies, and particularly at 10 kHz, large deviations in the directivity pattern occur for the nearest-neighbour and trilinear approximants. At 5 kHz, the numerical directivity is a better match, except in the case of the nearest-neighbour approximant to the longitudinal quadrupole.

As two final examples, consider the directivity of a longitudinal quadrupole at 10 kHz, under various choices of the quadrupole angle $\theta_Q = \hat{\theta}_Q$, and for a fractional index of $\xi_S = [-\frac{1}{2}, 0, -\frac{1}{2}]$. See Figure 11, illustrating the dependence of directivity on the fractional index. Though the numerical directivity patterns should be simple rotations of one another, considerable variation is seen in results from the nearest-neighbour and trilinear approximants. The optimised approximant with $N = 8$ exhibits virtually no such variation. Similarly, to examine the effects of displacement, consider the numerical directivity of a dipole under different choices of the fractional index ξ_S , as illustrated in Figure 12, showing a similar variation at 10 kHz. In this case, the phase $\angle(e^{-j\omega r/c} p_{\text{out}})$ of the approximation (removing the effects of propagation over a distance r) is compared to the exact phase $\angle(e^{-j\omega r/c} p_{\text{exact}})$, similarly showing variation with the fractional index.

D. Moving Monopole and Doppler Shifts

If a source is dynamic (or able to move or rotate during the course of a simulation) then the simulation as a whole becomes linear and time-variant. Fully frequency domain approaches to source modeling are no longer strictly valid. Pure spatio-temporal source designs, however, remain viable. Moving

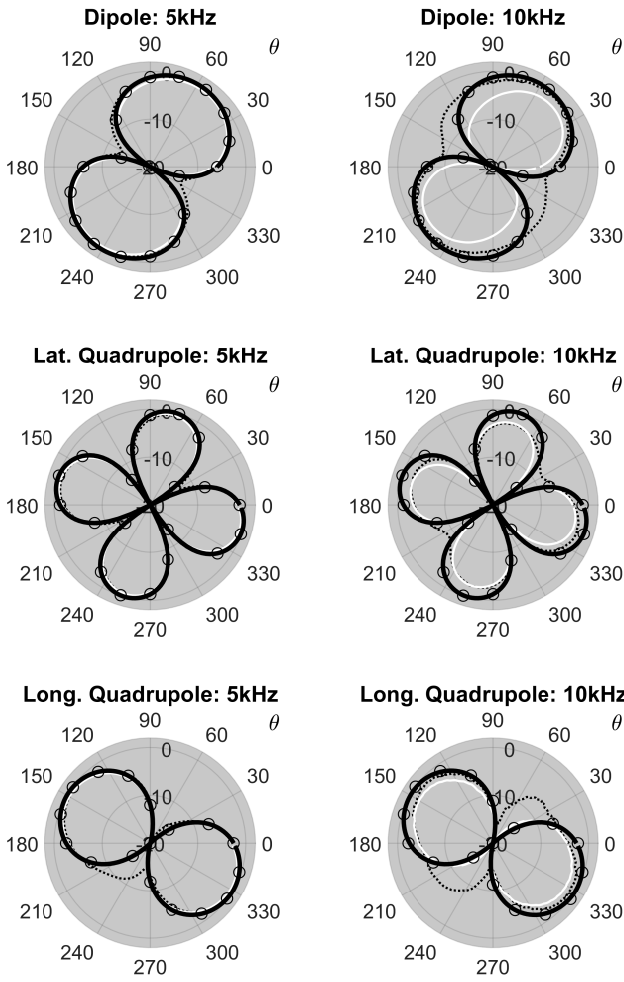


Fig. 10: Normalised multipole directivity as a function of θ , for $\phi = \pi/2$, at 5 kHz (left column) and 10 kHz (right column), for approximants to a dipole, with $[\phi_D, \theta_D] = [\pi/2, \pi/3]$, a lateral quadrupole, with $[\phi_Q, \theta_Q] = [\pi/2, \pi/6]$ and $[\phi_Q, \theta_Q] = [\pi/2, 5\pi/3]$, and a longitudinal quadrupole, with $[\phi_Q, \theta_Q] = [\phi_Q, \theta_Q] = [\pi/2, 11\pi/6]$. The exact directivity pattern is shown (solid black), along with a nearest-neighbour approximation (dotted), trilinear approximant (white) and an 8th-order separable approximant optimised with $\zeta = 0.6$ (circles).

sources obviously play a central role in auralisations, and it is of interest to present a basic simulation result here.

As a simple example of the effects of such approximants in a dynamic setting, consider a monopole source, moving along a linear trajectory at a constant velocity relative to a fixed receiver. The source excitation is a ramped sinusoid, at a frequency of 1 kHz, as shown at top in Figure 13 and travels at a velocity of $c/4 \text{ m} \cdot \text{s}^{-1}$; the velocity is chosen to be relatively high in order to illustrate Doppler shifting in the resulting outputs, drawn using a fixed omnidirectional receiver. Results using three different source approximants are illustrated. If nearest neighbour truncation is used, then severe distortion in the resulting waveform is observed, due to periodic jumps in the source location. Such distortion is greatly minimised in the case of the trilinear approximant, and not apparent in the case of a 12th-order optimised approximant to the monopole.

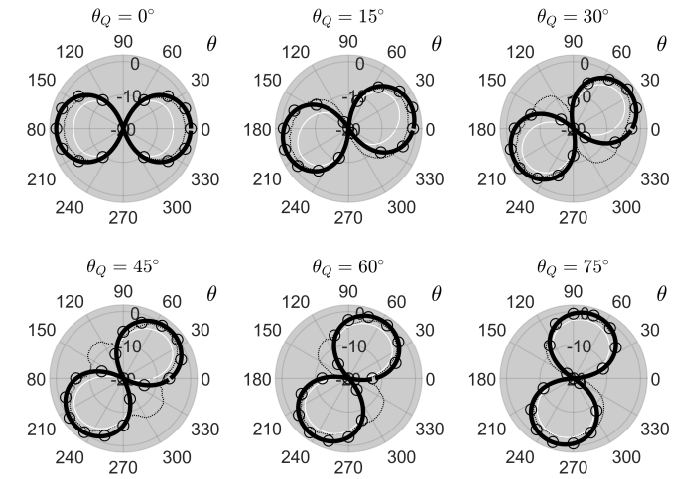


Fig. 11: Normalised directivity plots for a longitudinal quadrupole as a function of θ , for $\phi_Q = \pi/2$, and for various rotations θ_Q , as indicated. The exact directivity pattern is shown (solid black), along with a nearest-neighbour approximation (dotted), trilinear approximant (white) and an 8th-order separable approximant (circles).

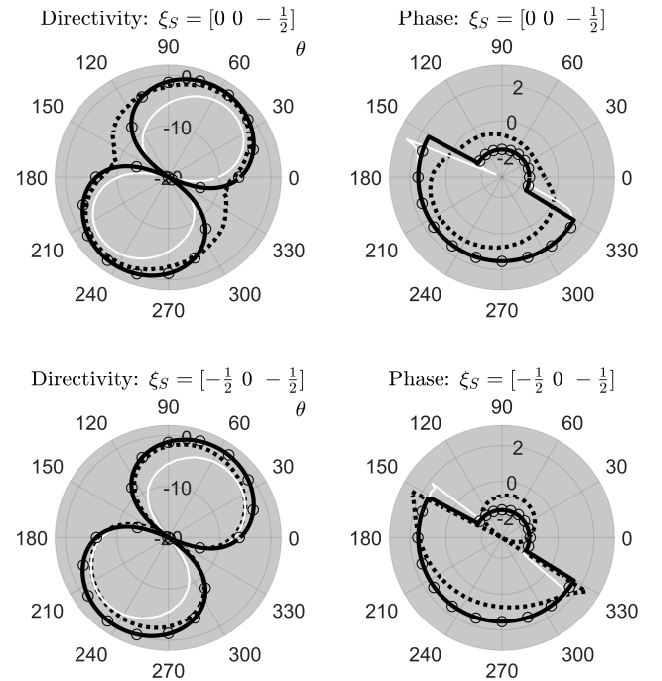


Fig. 12: Normalised directivity plots (left) and phase (right) for a dipole at 10 kHz, as a function of θ , for $\phi = \pi/2$, and for various rotations $[\phi_D, \theta_D] = [\pi/2, \pi/3]$. The exact directivity pattern is shown (solid black), along with a nearest-neighbour approximation (dotted), trilinear approximant (white) and an 8th-order separable approximant (circles). Results are shown for two choices of the fractional grid index ξ_S , as indicated.

VII. CONCLUDING REMARKS

This article has been concerned with the accurate simulation of source terms in FDTD schemes for the 3D wave equation. Sources are represented here as additional forcing terms in the 3D wave equation, and modeled as the product of an input signal and some combination of the Dirac distribution and its derivatives. In this way, point sources of arbitrary directivity may be modeled. Various strategies for approx-

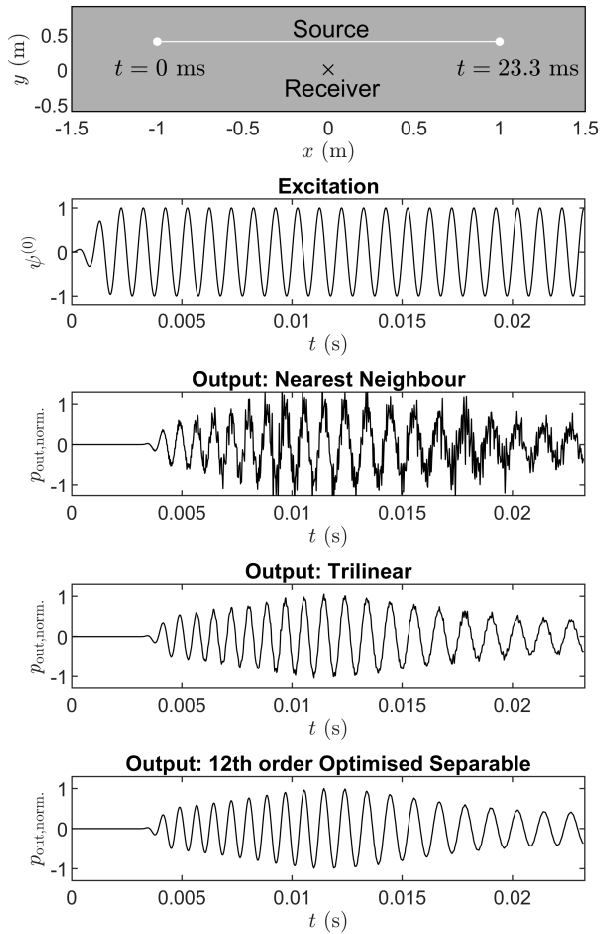


Fig. 13: Moving monopole relative to fixed receiver, over a trajectory indicated in the top panel (with $z = 0$ for both source and receiver), and with $\psi^{(0)}$ chosen as a windowed sinusoidal function, as indicated in the second panel. Omnidirectional output, drawn from a fixed receiver location is shown in the case of a nearest neighbour approximation (third panel), trilinear approximation (fourth panel) and using a 12th-order optimised approximant (bottom panel).

imating these forcing distributions over a grid have been presented here: nearest-neighbour and trilinear approximants, which are relatively simple to construct, produce reasonable results for low-frequency excitation, in terms of both the coherence of computed responses and directivity, as is to be expected. At higher frequencies, the behaviour of such approximants degrades considerably, and more general optimised forms constitute an approach to obtaining improved accuracy over a wider frequency range. The choice of approximant is necessarily governed by the properties of the numerical scheme used to approximate the 3D wave equation. A high-accuracy design has been employed here in order to show clearly the differences among approximation types, but if one were to use a simpler design (such as, e.g., the seven-point scheme mentioned in Section V), then such differences are small over the usable range of the scheme (i.e., at frequencies below which numerical dispersion becomes problematic). The

basic construction techniques presented here, however, are independent of the particular choice of scheme.

A major benefit of a local spatio-temporal representation of a source is the ability to render moving or rotating sources during the course of a simulation, without the need for a complete offline recalculation incorporating the entire room geometry—as is the case, e.g., in methods of a global character such as boundary element methods (BEM), for example [40]. The results in this article are geared towards allowing such flexibility, and a basic example showing the importance of good approximants in the case of moving sources has been illustrated in Section VI-D. For local methods such as those presented here, the approximant needs to be recalculated once per time step, incurring a cost scaling with the number of grid points over which the approximant is defined (and possibly a linear system solution in the case of optimised approximants). Though such a cost is not small, it is almost certainly negligible compared to the cost of simulation of the scheme over the entire problem domain for realistic room volumes at typical audio sampling frequencies. Remaining major issues, in the linear and time-varying case, are the assessment of the perceptual effects of the approximant, and the necessary accuracy required in order to render sources able to move and rotate as will be required in full virtual acoustic auralisations.

APPENDIX A

TENSOR DEFINITIONS AND IDENTITIES

A q th-order tensor \mathbf{A}_γ may be indexed by a q vector $\gamma = [\gamma_1, \dots, \gamma_q]$; in the present context of 3D acoustics, $\gamma_l = 1, 2, 3$, $l = 1, \dots, q$. A scalar element of \mathbf{A} with index γ will be indicated as $A_{\gamma_1, \dots, \gamma_q}$; in this work, $A_{\gamma_1, \dots, \gamma_q}$ can be either a value or a differential operator.

A q -fold contracted inner product between two q tensors \mathbf{A} and \mathbf{B} may be written as

$$\mathbf{A}^{(q)} \cdot \mathbf{B} = \sum_{\gamma_1=1}^3 \dots \sum_{\gamma_q=1}^3 A_{\gamma_1, \dots, \gamma_q} B_{\gamma_1, \dots, \gamma_q} \quad (68)$$

and is a scalar.

Given a vector $\mathbf{a} = [a_1, a_2, a_3]$, a q th-order tensor $\mathbf{A} = \mathbf{a}^q$ may be constructed using q powers of the vector \mathbf{a} , as

$$A_{\gamma_1, \dots, \gamma_q} = \prod_{l=1}^q a_{\gamma_l}. \quad (69)$$

The following identity holds, for any vectors \mathbf{a} and \mathbf{b} :

$$(\mathbf{a} \cdot \mathbf{b})^q = \mathbf{a}^{(q)} \cdot \mathbf{b}^q. \quad (70)$$

REFERENCES

- [1] L. Savioja, T. Rinne, and T. Takala. Simulation of room acoustics with a 3-D finite-difference mesh. In *Proc. Int. Comp. Music Conf.*, pages 463–466, Århus, Denmark, sep 1994.
- [2] D. Botteldooren. Acoustical finite-difference time-domain simulation in a quasi-cartesian grid. *J. Acoust. Soc. Am.*, 95(5):2313–2319, 1994.
- [3] D. Botteldooren. Finite-difference time-domain simulation of low-frequency room acoustic problems. *J. Acoust. Soc. Am.*, 98(6):3302–3308, 1995.

- [4] A. Krokstad, S. Strom, and S. Sorsdal. Calculating the acoustical room response by the use of a ray tracing technique. *J. Sound Vib.*, 8(1):118–125, 1968.
- [5] J. Allen and D. Berkley. Image method for efficiently simulating small-room acoustics. *J. Acoust. Soc. Am.*, 66(4):943–950, 1979.
- [6] A. Southern, D.T. Murphy, G. Campos, and P. Dias. Finite difference room acoustic modelling on a general purpose graphics processing unit. In *Proc. 128th Audio Eng. Soc. Conv.*, 2010.
- [7] J. Sheaffer and B. Fazenda. FDTD/K-DWM simulation of 3d room acoustics on generalpurpose graphics hardware using compute unified device architecture (CUDA). *Proc. Inst. Acoust.*, 32(5), 2010.
- [8] C. J. Webb and S. Bilbao. Computing room acoustics with CUDA - 3D FDTD schemes with boundary losses and viscosity. In *Proc. IEEE Int. Conf. Acoust., Speech Signal Proces.*, pages 317–320, 2011.
- [9] B. Hamilton. *Finite Difference and Finite Volume Methods for Wave-based Modelling of Room Acoustics*. PhD thesis, Acoustics and Audio Group, University of Edinburgh, 2016.
- [10] K. Yee. Numerical solution of initial boundary value problems involving Maxwell’s equations in isotropic media. *IEEE Trans. Antennas Propagation*, 14:302–307, 1966.
- [11] A. Taflov. *Computational Electrodynamics*. Artech House, Boston, Massachusetts, 1995.
- [12] C. Adamsson J. Nordstrom, K. Forsberg and P. Eliasson. Finite volume methods, unstructured meshes and strict stability. *Applied Numerical Mathematics*, 45:453–473, 2003.
- [13] R. Leveque. *Finite Volume Methods for Hyperbolic Problems*. Cambridge University Press, Cambridge, UK, 2002.
- [14] S. Bilbao. Modeling of complex geometries and boundary conditions in finite difference/finite volume time domain room acoustics simulation. *IEEE Trans. Audio Speech Language Proces.*, 21(7):1524–1533, 2013.
- [15] S. Bilbao, B. Hamilton, J. Botts, and L. Savioja. Finite volume time domain room acoustics simulation under general impedance boundary conditions. *IEEE/ACM Trans. Audio Speech Language Proces.*, 24(1):161–173, 2016.
- [16] M. Hornikx, W. De Roeck, and W. Desmet. A multi-domain Fourier pseudospectral time-domain method for the linearized Euler equations. *J. Comp. Phys.*, 231(14):4759–4774, 2012.
- [17] R. Mehra, N. Raghuvanshi, L. Savioja, M. Lin, and D. Manocha. An efficient GPU-based time domain solver for the acoustic wave equation. *Appl. Acoust.*, 73(2):83–94, 2012.
- [18] J. Botts, A. Bockman, and N. Xiang. On the selection and implementation of sources for finite-difference methods. In *Proc. 20th Int. Congr. Acoust.*, Sydney, Australia, 2010.
- [19] J. Sheaffer, M. van Walstijn, and B. Fazenda. Physical and numerical constraints in source modeling for finite difference simulation of room acoustics. *J. Acoust. Soc. Am.*, 135(1), 2014.
- [20] H. Jeong and Lam Y. Source implementation to eliminate low-frequency artifacts in finite difference time domain room acoustic simulation. *J. Acoust. Soc. Am.*, 258–268(1):1112–1118, 2012.
- [21] C. L. Wagner J. B. Schneider and S. L. Broschat. Implementation of transparent sources embedded in acoustic finite-difference time domain-grids. *J. Acoust. Soc. Am.*, 136–142(1):3219–3226, 1998.
- [22] D. Murphy, A. Southern, and L. Savioja. Source excitation strategies for obtaining impulse responses in finite difference time domain room acoustics simulation. *Appl. Acoust.*, 82:6–14, 2014.
- [23] A. Southern and D. Murphy. Low complexity directional sound sources for finite difference time domain room acoustic models. In *Proc. 126th Audio Eng. Soc. Conv.*, Munich, Germany, 2009.
- [24] J. Escolano, J. Lopez, and B. Pueo. Directive sources in acoustic discrete-time domain simulations based on directivity diagrams. *JASA Express Lett.*, 121:256–262, 2007.
- [25] H. Hacıhabiboglu, B. Günel, and Z. Cvetković. Simulation of directional microphones in digital waveguide mesh-based models of room acoustics. *IEEE Trans. Audio Speech Language Proces.*, 18(2):213–223, 2010.
- [26] J. Sheaffer, M. van Walstijn, B. Rafaely, and K. Kowalczyk. Binaural reproduction of finite difference simulations using spherical array processing. *IEEE/ACM Trans. Audio, Speech, Language Proces.*, 23(12):2125–2135, 2015.
- [27] F. Georgiou and M. Hornikx. Incorporating directivity in the fourier pseudospectral time-domain method using spherical harmonics. *J. Acoust. Soc. Am.*, 140:855–865, 2016.
- [28] A. Pierce. *Acoustics: An introduction to its physical principles and applications*. Acoustical Society of America, 1991.
- [29] X. Yang, X. Zhang, Z. Li, and G. He. A smoothing technique for discrete delta functions with application to immersed boundary method in moving boundary simulations. *J. Comp. Phys.*, 228:7821–7836, 2009.
- [30] N. Petersson, O. O’Reilly, B. Sjögreen, and S. Bydlon. Discretizing singular point sources in hyperbolic wave propagation problems. *J. Comp. Phys.*, 321:532–555, 2016.
- [31] S. Bilbao and B. Hamilton. Directional source modeling in wave based room acoustics simulation. In *Proc. IEEE Workshop Appl. Sig. Proces. Audio Acoust.*, New Paltz, New York, 2017.
- [32] P. Morse and U. Ingard. *Theoretical Acoustics*. Princeton University Press, Princeton, New Jersey, 1968.
- [33] B. Hosseini, N. Nigam, and J. Stockie. On regularizations of the Dirac delta distribution. *J. Comp. Phys.*, 305:423–447, 2016.
- [34] J. Strikwerda. *Finite Difference Schemes and Partial Differential Equations*. Wadsworth and Brooks/Cole Advanced Books and Software, Pacific Grove, California, 1989.
- [35] B. Gustafsson, H.-O. Kreiss, and J. Oliger. *Time Dependent Problems and Difference Methods*. John Wiley and Sons, New York, 1995.
- [36] B. Hamilton and S. Bilbao. FDTD methods for 3-D room acoustics simulation with high-order accuracy in space and time. *IEEE Trans. Audio Speech Lang. Proces.*, 25(11):2112–2124, 2017.
- [37] S. Bilbao and B. Hamilton. Higher-order accurate two-step finite difference schemes for the many dimensional wave equation. *J. Comp. Phys.*, 367:134–165, 2018.
- [38] G. R. Shubin and J. B. Bell. A modified equation approach to constructing fourth order methods for acoustic wave propagation. *SIAM J. Sci. Stat. Comp.*, 8:135–51, 1987.
- [39] M. Dablain. The application of high-order differencing to the scalar wave equation. *Geophysics*, 51(1):54–66, 1986.
- [40] T. Sakuma, S. Sakamoto, and T. Otsuru, editors. *Computational Simulation in Architectural and Environmental Acoustics*. Springer Japan, Tokyo, 2014.

Stefan Bilbao Stefan Bilbao (B.A. Physics, Harvard, 1992, MSc., PhD Electrical Engineering, Stanford, 1996 and 2001 respectively) is currently Professor of Acoustics and Audio Signal Processing in the Acoustics and Audio Group at the University of Edinburgh, and previously held positions at the Sonic Arts Research Centre, at the Queen’s University Belfast, and the Stanford Space Telecommunications and Radioscience Laboratory. He has led the NESS project (Next Generation Sound Synthesis) and WRAM project (Wave-based Room Acoustics Modeling), both funded by the European Research Council, and running jointly between the Acoustics and Audio Group and the Edinburgh Parallel Computing Centre at the University of Edinburgh between 2012 and 2018. He was born in Montreal, Quebec, Canada.

Brian Hamilton Brian Hamilton (M’09) received B.Eng. (Hons.) and M.Eng. degrees in electrical engineering from McGill University, Montreal, QC, Canada, in 2009 and 2012, respectively, and the Ph.D. degree from the University of Edinburgh, Edinburgh, U.K., in 2016, as part of the NESS project (Next Generation Sound Synthesis), funded by the European Research Council (ERC). He is currently a Postdoctoral Research Fellow in the Acoustics and Audio Group at the University of Edinburgh, as part of the ERC-funded project WRAM (Wave-based Room Acoustic Modelling). His research interests include numerical methods for 3-D room acoustics simulations and spatial audio.